Digit. Signal Process. 170 (2026) 105795

Contents lists available at ScienceDirect

Digital Signal Processing

journal homepage: www.elsevier.com/locate/dsp

Array geometry optimization with excitation quantization constraints: A mixed-integer programming approach

Xue Shi [a], Xuejing Zhang [b,*], Cheng Liu [b], Xuepan Zhang [c]

[a] College of Computer Science and Cyber Security, Chengdu University of Technology, Chengdu, Sichuan, China
[b] School of Information and Communication Engineering, University of Electronic Science and Technology of China, Chengdu, Sichuan, China
[c] Hangzhou Institute of Technology, Xidian University, Hangzhou, Zhejiang, China

ARTICLE INFO

Keywords:
Array geometry optimization
Array pattern synthesis
Excitation quantization
Mixed-integer programming
Quantization sidelobe
Phased array

ABSTRACT

This paper addresses the problem of array geometry optimization, with a specific focus on array layout designs that incorporate phase and/or amplitude quantization constraints applied to the excitation. By jointly optimizing the antenna selection states and position offsets, we introduce a continuous antenna selection scheme and develop a framework for array geometry optimization using mixed integer programming (MIP). Our method is applicable to both one-dimensional linear arrays and two-dimensional planar arrays, and accommodates a wide range of pattern synthesis scenarios with excitation quantization constraints. Moreover, the proposed method supports multi-objective optimization for array geometry design. In this paper, we investigate linearization and equivalent reformulation techniques across different array geometry optimization scenarios, thereby obtaining tractable MIP models that can be effectively solved using off-the-shelf solvers. Theoretical analysis is provided to support the rationality of our approach. Extensive simulations are conducted to demonstrate the effectiveness and superiority of the proposed method, validating its performance under various scenarios.

1. Introduction

Array geometry optimization is a crucial aspect of antenna array design and plays a vital role in enhancing the performance of radar, communication, and other systems that rely on antenna arrays [1]. In array geometry optimization, we primarily focus on optimizing the position and spacing of the antenna elements within the array [2]. In radar systems, optimizing the array geometry can improve the angular resolution, reduce sidelobe levels, and enhance detection and tracking capabilities [3]. In some communication systems, optimizing the array geometry can improve the spectral efficiency, and facilitate better spatial diversity and multiplexing gains. Generally, through the optimization of array geometry, the system's capabilities can be significantly enhanced across various aspects, ultimately resulting in superior overall performance [4].

Over the past few decades, numerous array geometry optimization methods have been proposed, aiming to radiate the desired beampatterns. A classic array geometry optimization algorithm is implemented using evolutionary approach. It primarily utilizes techniques such as simulated annealing [5], particle swarm optimization [6], and genetic algorithm [7]. These algorithms are inspired by natural selection and statistical mechanics principles, and can take into account practical constraints in array geometry optimization. However, the effectiveness of these algorithms is sensitive to parameter selection. Another representative approach is to perform array geometry optimization based on a specified reference beampattern. It mainly includes the matrix pencil method in [8] and the sparse Bayesian learning (SBL) method in [9]. These two methods demonstrate good potential for array geometry optimization, especially in sparse array design. However, they require the specification of reference array and reference beampattern, and there is currently no theoretical basis for determining the optimal reference array/beampattern. Recently, an array geometry optimization algorithm based on low-rank matrix completion has been proposed in [10], and it does not require the setting of reference array/beampattern. The drawback of this algorithm is that it cannot incorporate practical constraints for array geometry optimization.

With the rise of convex optimization theory [11], it has been successfully applied to array geometry design. The authors of [12] investigate how to achieve array geometry optimization by selecting antennas from a set of candidates, and utilize convex programming (CP) to find the solution. Building on the idea of antenna selection, some works have considered how to incorporate practical array constraints into array geometry optimization, thereby enabling flexible array geometry design through CP. For instance, the reference [13] explores how to design array geometry optimization under the constraint of minimum

* Corresponding author.
E-mail address: xjzhang7@163.com (X. Zhang).

https://doi.org/10.1016/j.dsp.2025.105795

Available online 7 December 2025

antenna spacing. In [14], the array geometry is designed under a given shape constraint on beampattern. It should be pointed out that the above methods select antennas from a given set of candidates, and it limits the freedom of array geometry design due to the fact that the candidate grid is discrete rather than continuous. Although it is possible to approximate continuous array geometry design by reducing the spacing between candidate antennas, this approach would significantly increase computational complexity and is prone to resulting in excessively small element spacings [15].

To address the above grid constraint issue, some recent works have considered continuous array geometry design. For instance, given a specified amplitude excitation, the authors of [16] employ a Taylor series expansion to derive a simplified approximate expression related to the array element position parameters, which is then iteratively solved to achieve array geometry optimization. Similarly, the reference [17] investigates how to minimize the number of array elements across various scenarios through array geometry optimization, while also enhancing the robustness of the array design. It is important to note that both of these methods require iterative solutions and often necessitate the specification of initial positions for the array elements [18]. Another approach to continuous array geometry design is the deterministic synthesis method [19–21]. Although these methods can provide an analytical expression for computing the inter-element spacing, they suffer from limited flexibility and often cannot be easily adjusted according to practical applications. Additionally, continuous array geometry optimization can also be realized through techniques such as off-grid compressed sensing [22], atomic norm minimization [23], and deep learning [24–26].

It is worth noting that the aforementioned array geometry optimization methods do not consider the quantization effects on excitation phase and amplitude. In practical applications, array systems employ digital phase shifters and digital attenuators to control the excitation phase and amplitude, respectively. Owing to the limited precision of digital devices, quantization becomes necessary, which can result in a finite number of possible states for the excitations and introduce quantization sidelobe on the radiation beampattern. Given a predetermined array geometry, there has been several research on beampattern synthesis considering quantization constraints [27–29]. Nevertheless, the problem of array geometry optimization under excitation quantization constraints has received limited attention. To our knowledge, the only existing work is our previously proposed sparse array synthesis method that considers phase quantization, as presented in [30]. However, this method only considers phase quantization and is subject to the aforementioned grid issues.

To address the deficiencies of existing methods, in this paper we consider the joint design of element positions and excitations in the presence of quantization constraints. We found that the problem of array geometry optimization under excitation quantization constraints can be effectively modeled via mixed-integer programming (MIP). Unlike traditional antenna selection schemes, we present a continuous antenna selection approach by introducing offsets to the candidate antennas. Through joint optimization of antenna selection states and the corresponding offsets, our method enhances design freedom, allowing for more precise and flexible array geometry design. More importantly, the proposed scheme takes into account the quantization constraints of the excitations, including both excitation phase and excitation amplitude, leading to more satisfactory beampattern results. In this paper, we consider the array geometry optimization problems for various scenarios, and utilize MIP techniques to reformulate the complex constraints into tractable forms that can be solved using off-the-shelf solvers, such as Gurobi [31] and CPLEX [32]. The main contributions of this paper can be summarized as follows:

1. We propose an array geometry optimization framework that considers the constraints of excitation quantization (including both excitation phase and excitation amplitude), utilizing mixed-integer programming. By introducing positional offsets to the candidate antennas, our method can achieve accurate and flexible array geometry design. We provide some theoretical analysis to support the rationality of the proposed method.
2. The proposed scheme is applicable to various array geometry optimization scenarios and is suitable for both one-dimensional linear arrays and two-dimensional planar arrays. In addition, our method can realize multi-objective optimization for array geometry design.
3. Leveraging MIP modeling techniques, we equivalently linearize and reformulate the complex models into tractable ones, which can be solved using off-the-shelf solvers. Furthermore, we conduct simulations to validate the proposed method under various scenarios, and the results demonstrate its effectiveness and superiority.

The rest of the paper is organized as follows. In Section 2, we introduce some preliminaries on array geometry optimization and excitation quantization. In Section 3, we present the proposed array geometry optimization method under phase quantization constraint. Extensions to other scenarios are presented in Section 4. Simulation results are shown in Section 5 and conclusions are drawn in Section 6.

Notations: We use bold upper-case and lower-case letters to represent matrices and vectors, respectively. In particular, we use $\mathbf{1}$ and $\mathbf{0}$ to represent all-one vector and all-zero vector respectively, where the vector dimension is specified by the subscript or inferred from the context. $(\cdot)^T$ denotes the transpose operation, $|\cdot|$ calculates absolute value and $\angle(\cdot)$ returns the argument of the input. We use $\{0,1\}$ to denote the set of binary elements (where each element can only take either 0 or 1). The notation $\odot$, $\otimes$, and $\oslash$ denote the Hadamard product, Kronecker product, and the element-wise division operation, respectively. We use $\|\cdot\|_\beta$ to denote norm of the input vector (with the specific type specified by the subscript β). The notation $\mathrm{vec}(\cdot)$ represents the vectorization operation on a matrix, and $\mathrm{Diag}(\cdot)$ returns a diagonal matrix generated by the input vector. We use the notations $\preceq$ and $\succeq$ to represent element-wise comparison between matrices. For example, $\boldsymbol{A} \preceq \boldsymbol{B}$ implies that each element of $\boldsymbol{A}$ is not greater than the corresponding element of $\boldsymbol{B}$ in the same position.

2. Preliminaries

In this section, we present some preliminaries on array geometry optimization and excitation quantization. For simplicity, we focus on the one-dimensional linear arrays with isotropic antennas, although the extension to more complex scenarios (such as arrays with non-isotropic elements) is applicable as well.

2.1. Array geometry optimization

Under the assumption of far-field and narrowband, the array response for an N-element linear array is defined as

$$f(\boldsymbol{p},\theta) \triangleq \boldsymbol{w}^T \boldsymbol{a}(\boldsymbol{p},\theta) \tag{1}$$

where $\boldsymbol{w} = [w_1, \cdots, w_N]^T$ represents the complex excitation vector, $\boldsymbol{a}(\boldsymbol{p},\theta)$ is the steering vector for the spatial angle θ and is defined as

$$\boldsymbol{a}(\boldsymbol{p},\theta) \triangleq [e^{-j(2\pi/\lambda)p_1\sin(\theta)}, \cdots, e^{-j(2\pi/\lambda)p_N\sin(\theta)}]^T. \tag{2}$$

In (2), $\boldsymbol{p} = [p_1, \cdots, p_N]^T$ is the position vector for the array, λ represents wavelength. The array beampattern is typically described by the magnitude of array response, i.e., $|f(\boldsymbol{p},\theta)|$.

The primary goal of array geometry optimization is to systematically adjust the spatial arrangement of antenna elements within an array to maximize its overall performance and efficiency. In this paper, we specifically focus on optimizing the array geometry to enhance the beampattern performance.

2.2. Excitation quantization

For practical phased arrays, the excitation phase (i.e., $\angle w_n$, $n = 1, \cdots, N$) is typically controlled by the digital phase shifter. Considering

the finite resolution of digital phase shifter, for Q-bit phase quantization, the excitation phase is required to take values from the following finite set:

$$\Psi_Q \triangleq \{0, \varphi, 2\varphi, \cdots, (2^Q - 1)\varphi\} \tag{3}$$

where $\varphi = 2\pi/2^Q$ represents the phase resolution corresponding to the Q-bit phase quantization.

The excitation amplitude (i.e, $|w_n|$, $n = 1, \cdots, N$) of an antenna array is typically controlled by digital attenuators. For J-bit amplitude quantization, the excitation amplitude is required to take values from the following finite set [33]:

$$\Upsilon_J \triangleq \{\alpha_1^{(J)}, \alpha_2^{(J)}, \cdots, \alpha_{2^J}^{(J)}\} \tag{4}$$

where $\alpha_{2^J}^{(J)}$ (in decibels) represents the given dynamic range of the digital attenuator, the elements of Υ_J are calculated as $\alpha_i^{(J)} = (i-1) \cdot \alpha_{2^J}^{(J)}/(2^J - 1)$, $i = 1, \cdots, 2^J$. It should be noted that the elements of Υ_J are all described in decibels.

3. Array geometry optimization with phase quantization constraint

In this section, we investigate the problem of array geometry optimization under phase quantization constraint. We propose a continuous antenna selection scheme that enables precise and flexible design of antenna positions. Through linearization and reformulation, we derive a mixed-integer programming model, which can be solved using MIP solvers. Moreover, we present some theoretical analysis to support the rationality of the proposed method.

3.1. Continuous antenna selection for array geometry optimization

As a classic method for array geometry optimization, the antenna selection approach begins by compactly arranging M candidate antennas within a given aperture. The optimization of array geometry is then achieved by selecting some antennas from these candidate ones. Specifically, we denote $\bar{\boldsymbol{p}} = [\bar{p}_1, \cdots, \bar{p}_M]^T$, where $\bar{p}_m$ is pre-determined and represents the position coordinate of the mth candidate antenna, $m = 1, \cdots, M$.

Taking focused-beam synthesis as an example, assume that we select N antennas out of M to form the ultimate array. The objective of array geometry optimization is to obtain the lowest peak sidelobe level (PSL). Without considering the quantized constraints on excitations, the array geometry optimization can then be achieved by solving the following problem [30]:

$$\min_{\boldsymbol{w},\boldsymbol{b},\rho} \quad \rho \tag{5a}$$

$$\text{s.t.} \quad \boldsymbol{w}^T \boldsymbol{a}(\bar{\boldsymbol{p}}, \bar{\theta}_0) = 1 \tag{5b}$$

$$|\boldsymbol{w}^T \boldsymbol{a}(\bar{\boldsymbol{p}}, \theta)| \le \rho, \ \forall \theta \in \mathbb{S} \tag{5c}$$

$$|\boldsymbol{w}| \preceq \eta \cdot \boldsymbol{b} \tag{5d}$$

$$\mathbf{1}^T \boldsymbol{b} = N \tag{5e}$$

$$\boldsymbol{b} \in \{0, 1\}^M \tag{5f}$$

where $\bar{\theta}_0$ is the mainlobe axis, $\mathbb{S}$ stands for the sidelobe region, η is a sufficiently large positive constant, and we have implicitly assume that the maximum excitation amplitude does not exceed η.

Note that in the above formulation (5), $\boldsymbol{b}$ is a binary vector, i.e., its elements can only take the values of zero or one as indicated in (5f). According to (5d), it becomes evident that if an element of $\boldsymbol{b}$ equals zero, the value at the corresponding position in $\boldsymbol{w}$ must be zero as well. Then, the antenna at corresponding position can be removed. Conversely, when an element of $\boldsymbol{b}$ takes one, the corresponding element in $\boldsymbol{w}$ can takes non-zero values, and the antenna at corresponding position can be retained. In this way, we achieve array geometry optimization by designing whether to retain each antenna. The formulation (5) is a mixed-integer programming (MIP) problem, including both integer variable (see $\boldsymbol{b}$) and the continuous ones (see $\boldsymbol{w}$ and ρ). In fact, we can solve problem (5) using MIP solvers, such as Gurobi [31] and CPLEX [32].

It is important to note that in the aforementioned array geometry optimization scheme, the candidate antennas are typically distributed only on discrete grid points. This implies that antenna selection can only be performed from a finite set of given positions. Consequently, the above antenna selection scheme may not be able to achieve satisfactory performance on beampattern. Especially when excitation phase quantization need to be considered, the aforementioned scheme may yield poor results due to the limited degrees of freedom.

To enhance the design freedom in array geometry optimization, we introduce position offsets to the candidate antennas while performing antenna selection. Specifically, after adding a small offset vector $\boldsymbol{\delta}$ to the position vector $\bar{\boldsymbol{p}}$ of the candidate antennas, we can approximate the steering vector as

$$\boldsymbol{a}(\bar{\boldsymbol{p}} + \boldsymbol{\delta}, \theta) \approx \boldsymbol{a}(\bar{\boldsymbol{p}}, \theta) + \boldsymbol{\delta} \odot \boldsymbol{a}'(\bar{\boldsymbol{p}}, \theta) \tag{6}$$

where $\boldsymbol{\delta} = [\delta_1, \cdots, \delta_M]^T$ is utilized to characterize the position offset of each candidate antenna, $\boldsymbol{a}'(\bar{\boldsymbol{p}}, \theta)$ is the derivative vector evaluated at $\bar{\boldsymbol{p}}$, which can be represented as

$$\boldsymbol{a}'(\bar{\boldsymbol{p}}, \theta) = \left[\frac{\partial e^{-j(2\pi/\lambda)\bar{p}_1 \sin(\theta)}}{\partial \bar{p}_1} \quad \cdots \quad \frac{\partial e^{-j(2\pi/\lambda)\bar{p}_M \sin(\theta)}}{\partial \bar{p}_M} \right]^T.$$

In fact, eqrefkdfjalftal can be regarded as the first-order Taylor expansion of $\boldsymbol{a}(\bar{\boldsymbol{p}} + \boldsymbol{\delta}, \theta)$ at $\bar{\boldsymbol{p}}$, where it is essential to ensure that the offset $\boldsymbol{\delta}$ is sufficiently small [34].

Based on the aforementioned approximation (6), we can achieve array geometry optimization through continuous antenna selection. Fig. 1 illustrates the schematic diagram of continuous antenna selection when $M = 8$ and $N = 5$. Specifically, due to the introduction of the position offset $\boldsymbol{\delta}$ and the linearity of the right-hand side of (6) with respect to $\boldsymbol{\delta}$, we can further design the displacement of the selected antennas on the basis of setting the antenna selection state (removal or retention). Since the offset vector can take continuous values, this allows us to perform fine and flexible array geometry optimization in a continuous space.

Before delving further into the discussion of the proposed array geometry optimization method, we define the approximate array response corresponding to the candidate array (with position offset) as

$$z(\bar{\boldsymbol{p}}, \theta) \triangleq \boldsymbol{w}^T [\boldsymbol{a}(\bar{\boldsymbol{p}}, \theta) + \boldsymbol{\delta} \odot \boldsymbol{a}'(\bar{\boldsymbol{p}}, \theta)]. \tag{7}$$

The above $z(\bar{\boldsymbol{p}}, \theta)$ serves as an approximation to the nominal array response $f(\bar{\boldsymbol{p}}, \theta) = \boldsymbol{w}^T \boldsymbol{a}(\bar{\boldsymbol{p}}, \theta)$. Define the approximation error at a given spatial angle θ as

$$e(\theta) \triangleq \Big| |z(\bar{\boldsymbol{p}}, \theta)| - |f(\bar{\boldsymbol{p}}, \theta)| \Big|. \tag{8}$$

It can be proved that for any $\boldsymbol{p}$, $\boldsymbol{\delta}$ and $\boldsymbol{w}$, $e(\theta)$ satisfies

$$e(\theta) \le \underbrace{\frac{2\pi^2 \sin^2(\theta)}{\lambda^2} \|\boldsymbol{w}\|_{\beta_1} \cdot \|\boldsymbol{\delta} \odot \boldsymbol{\delta}\|_{\beta_2}}_{\triangleq r(\theta)} \tag{9}$$

where β_1 and β_2 can be any positive numbers as long as they satisfy $\frac{1}{\beta_1} + \frac{1}{\beta_2} = 1$. From (9), we can know that the maximum deviation between the approximate beampattern and the nominal one is bounded by $r(\theta)$. The proof of (9) can be found in Appendix A.

3.2. Continuous antenna selection with phase quantization constraint

In practical applications, the quantization of phase shifters can reduce costs and complexity. Under phase quantization, excitation phases are selected from a predefined set. Specifically, with Q-bit phase quantization and $L = 2^Q$, we can enumerate candidate phases to form the following vector $\boldsymbol{c}$:

$$\boldsymbol{c} = [1, e^{j2\pi/L}, \cdots, e^{j2(L-1)\pi/L}]^T. \tag{10}$$

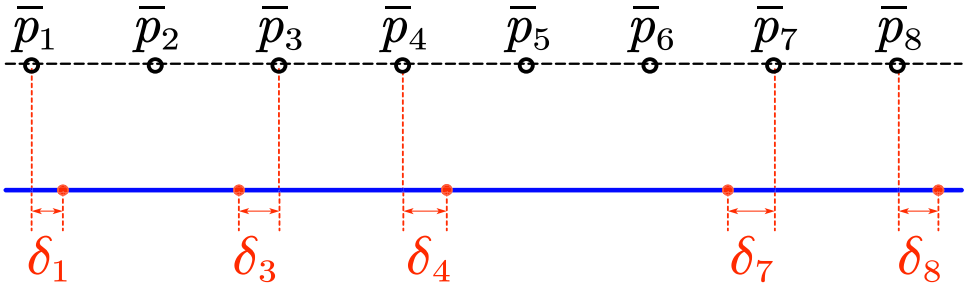

Fig. 1. Schematic diagram of continuous antenna selection when $M = 8$ and $N = 5$.

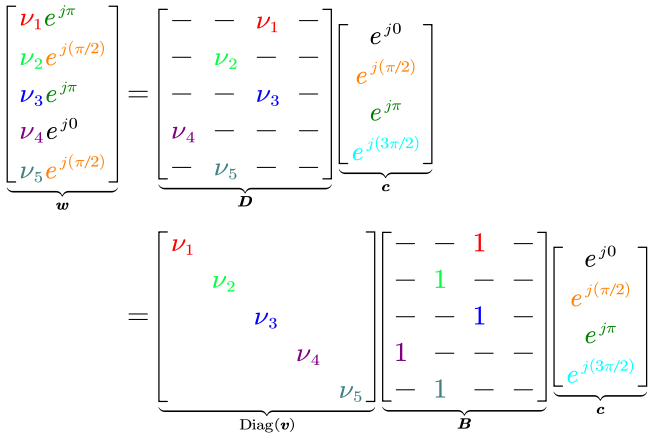

Fig. 2. A more detailed illustration of (14) with $M = 5$ and $Q = 2$.

Introducing an $M \times L$ matrix $\boldsymbol{D}$ to indicate the excitation amplitude, we can express the weight vector under phase quantization as

$$\boldsymbol{w} = \boldsymbol{D}\boldsymbol{c} \tag{11}$$

where the entries of $\boldsymbol{D}$ are non-negative, i.e., $\boldsymbol{D} \geq \boldsymbol{0}$. Since $\boldsymbol{c}$ is pre-assigned, the design of $\boldsymbol{w}$ can be converted to the design of $\boldsymbol{D}$ with appropriate constraints. In this way, the phase quantization constraint can be always satisfied.

Considering the array geometry optimization scenario described in (5), we can similarly introduce a binary matrix $\boldsymbol{B}$ and add the following constraints on $\boldsymbol{D}$ and $\boldsymbol{B}$:

$$\boldsymbol{0} \preceq \boldsymbol{D} \preceq \eta \cdot \boldsymbol{B} \tag{12a}$$
$$\boldsymbol{B}\boldsymbol{1} \preceq \boldsymbol{1} \tag{12b}$$
$$\boldsymbol{1}^T \boldsymbol{B}\boldsymbol{1} = N \tag{12c}$$
$$\boldsymbol{B} \in \{0,1\}^{M \times L} \tag{12d}$$

where the constraints (12a) and (12b) ensure that each row of the matrix $\boldsymbol{D}$ contains at most one positive element, which represents the excitation amplitude of the corresponding antenna. The constraint (12c) ensures that the number of selected antennas is N. In fact, under the above constraint (12), if we define

$$\boldsymbol{v} \triangleq \boldsymbol{D}\boldsymbol{1} \tag{13}$$

it is not difficult to re-express $\boldsymbol{w}$ in (11) as

$$\boldsymbol{w} = \boldsymbol{D}\boldsymbol{c} = \mathrm{Diag}(\boldsymbol{v})\boldsymbol{B}\boldsymbol{c} \tag{14}$$

which facilitates our subsequent derivations. To have an intuitive understanding, Fig. 2 presents a more detailed illustration of (14) using an example with $M = 5$ and $Q = 2$.

We now proceed to further investigate how array geometry optimization can be achieved through the application of the continuous antenna selection approach presented in Section 3.1. In fact, when considering the constraint of excitation phase quantization, the continuous antenna selection scheme not only enhances design freedom and flexibility but also results in a tractable formulation. To illustrate this point, we substitute (14) into (6), and then express the approximated array response $z(\bar{\boldsymbol{p}}, \theta)$ corresponding to the candidate array (with position offset) as

$$z(\bar{\boldsymbol{p}}, \theta) = \boldsymbol{c}^T \boldsymbol{D}^T \boldsymbol{a}(\bar{\boldsymbol{p}}, \theta) + \underbrace{\boldsymbol{c}^T \boldsymbol{D}^T [\boldsymbol{\delta} \odot \boldsymbol{a}'(\bar{\boldsymbol{p}}, \theta)]}_{\triangleq \zeta(\boldsymbol{D}, \boldsymbol{\delta})}. \tag{15}$$

As previously described, both $\boldsymbol{D}$ and $\boldsymbol{\delta}$ need to be determined in the array geometry optimization.

To obtain a tractable constraint form, we define

$$\boldsymbol{x} \triangleq \boldsymbol{v} \odot \boldsymbol{\delta} \tag{16}$$
$$\boldsymbol{y} \triangleq (\boldsymbol{1} \otimes \boldsymbol{x}) \odot \mathrm{vec}(\boldsymbol{B}) \tag{17}$$
$$\boldsymbol{s}(\bar{\boldsymbol{p}}, \theta) \triangleq \boldsymbol{c} \otimes \boldsymbol{a}'(\bar{\boldsymbol{p}}, \theta). \tag{18}$$

Using (14), we can re-express $\zeta(\boldsymbol{D}, \boldsymbol{\delta})$ in (15) as follows:

$$\begin{aligned}
\zeta(\boldsymbol{D}, \boldsymbol{\delta}) &= \boldsymbol{c}^T \boldsymbol{D}^T (\boldsymbol{\delta} \odot \boldsymbol{a}') && \text{(19a)}\\
&= \boldsymbol{c}^T \boldsymbol{B}^T [\mathrm{Diag}(\boldsymbol{v})]^T (\boldsymbol{\delta} \odot \boldsymbol{a}') && \text{(19b)}\\
&= \boldsymbol{c}^T \boldsymbol{B}^T (\boldsymbol{v} \odot \boldsymbol{\delta} \odot \boldsymbol{a}') && \text{(19c)}\\
&= [\boldsymbol{c} \otimes (\boldsymbol{v} \odot \boldsymbol{\delta} \odot \boldsymbol{a}')]^T \mathrm{vec}(\boldsymbol{B}) && \text{(19d)}\\
&= [(\boldsymbol{1} \otimes \boldsymbol{x}) \odot (\boldsymbol{c} \otimes \boldsymbol{a}')]^T \mathrm{vec}(\boldsymbol{B}) && \text{(19e)}\\
&= [(\boldsymbol{1} \otimes \boldsymbol{x}) \odot \mathrm{vec}(\boldsymbol{B})]^T (\boldsymbol{c} \otimes \boldsymbol{a}') && \text{(19f)}\\
&= \boldsymbol{y}^T \boldsymbol{s}(\bar{\boldsymbol{p}}, \theta) && \text{(19g)}
\end{aligned}$$

where we have abbreviated $\boldsymbol{a}'(\bar{\boldsymbol{p}}, \theta)$ as $\boldsymbol{a}'$ in the above derivations. In (19d), we have utilized the matrix identity $\mathrm{vec}(\boldsymbol{U}\boldsymbol{V}\boldsymbol{W}) = (\boldsymbol{W}^T \otimes \boldsymbol{U})\mathrm{vec}(\boldsymbol{V})$.

Using the derived result in (15), we can re-express the array response in (15) as

$$z(\bar{\boldsymbol{p}}, \theta) = \boldsymbol{c}^T \boldsymbol{D}^T \boldsymbol{a}(\bar{\boldsymbol{p}}, \theta) + \boldsymbol{y}^T \boldsymbol{s}(\bar{\boldsymbol{p}}, \theta) \tag{20}$$

where $\boldsymbol{y}$ and $\boldsymbol{s}(\bar{\boldsymbol{p}}, \theta)$ are defined in (17) and (18), respectively. Then, based on the continuous antenna selection scheme, we can obtain the following array geometry optimization model:

$$\begin{aligned}
\min_{\boldsymbol{v},\boldsymbol{\delta},\boldsymbol{x},\boldsymbol{y},\boldsymbol{B},\boldsymbol{D},\rho} \quad & \rho && \text{(21a)}\\
\text{s.t.} \quad & z(\bar{\boldsymbol{p}}, \bar{\theta}_0) = 1 && \text{(21b)}\\
& |z(\bar{\boldsymbol{p}}, \theta)| \leq \rho, \ \forall \theta \in \mathbb{S} && \text{(21c)}\\
& \boldsymbol{0} \preceq \boldsymbol{D} \preceq \eta \cdot \boldsymbol{B} && \text{(21d)}\\
& \boldsymbol{B}\boldsymbol{1} \preceq \boldsymbol{1} && \text{(21e)}\\
& \boldsymbol{1}^T \boldsymbol{B}\boldsymbol{1} = N && \text{(21f)}\\
& \boldsymbol{v} = \boldsymbol{D}\boldsymbol{1} && \text{(21g)}\\
& \boldsymbol{x} = \boldsymbol{v} \odot \boldsymbol{\delta} && \text{(21h)}\\
& \boldsymbol{y} = (\boldsymbol{1} \otimes \boldsymbol{x}) \odot \mathrm{vec}(\boldsymbol{B}) && \text{(21i)}\\
& \|\boldsymbol{\delta}\|_\infty \leq \gamma && \text{(21j)}\\
& \boldsymbol{B} \in \{0,1\}^{M \times L} && \text{(21k)}
\end{aligned}$$

where (21j) is used to constrain the offset to be sufficiently small, with γ being a given positive constant. Unlike (5), we have considered the

constraint of excitation phase quantization in the above formulation. Moreover, due to the introduction of the offset vector $\boldsymbol{\delta}$, the above model allows for the design of element positions within a continuous space. In this way, the design freedom and flexibility can be improved, thereby aiming to achieve a lower PSL.

On the other hand, similar to model (5), the above model (21) encompasses both discrete variable (see variable $\boldsymbol{B}$) and continuous variable (all other variables except $\boldsymbol{B}$), thereby categorizing it as an MIP model. However, the model (21) includes intricate constraints that preclude its direct solving using MIP solvers. These primarily include the product constraints involving continuous variables as detailed in (21h), as well as product constraints between discrete and continuous variables as presented in (21i). In the next subsection, we apply linearization techniques from mixed-integer programming to reformulate (21) into an equivalent form, thereby eliminating the aforementioned intricate constraints.

3.3. Linearization and reformulation for model (21)

In this subsection, we derive a tractable reformulation for model (21) by performing equivalent transformations on the product constraints (21h) and (21i). We begin by first considering the product constraint (21h) between continuous variables.

According to the constraints (21d) and (21g), the elements of vector $\boldsymbol{v}$ are non-negative, and their maximum value does not exceed η. For the position offset vector $\boldsymbol{\delta}$, it follows from constraint (21j) that its elements take values within the interval $[-\gamma, \gamma]$. Obviously, the constraint (21h) indicates that the values of vector $\boldsymbol{x}$ are all within the interval $[-\eta\gamma, \eta\gamma]$. More importantly, once $\boldsymbol{x}$ and $\boldsymbol{v}$ are obtained, we can solve the vector $\boldsymbol{\delta}$ as

$$\boldsymbol{\delta} = \boldsymbol{x} \oslash \boldsymbol{v}. \tag{22}$$

It should be noted that the corresponding elements of $\boldsymbol{\delta}$ obtained from the above equation are meaningful only when a specific antenna is selected, i.e., when a certain element of the vector $\boldsymbol{v}$ takes a non-zero value. Therefore, we do not need to be concerned about the potential issue of the denominator in the above division being zero.

Since only the constraints (21h) and (21j) are directly related to $\boldsymbol{\delta}$, we can eliminate the vector $\boldsymbol{\delta}$ while retaining only $\boldsymbol{x}$ and $\boldsymbol{v}$. On this basis, the constraint (21h) needs to be revised to

$$|\boldsymbol{x}| \preceq \gamma \cdot \boldsymbol{v}. \tag{23}$$

At this point, solving for the vector $\boldsymbol{\delta}$ using (22) will still satisfy the original constraints (21h) and (21j). In this way, the original product constraint (21h) and the norm constraint (21j) can be eliminated. In fact, it can be known from constraint (21g) that the vector $\boldsymbol{v}$ is determined by the matrix $\boldsymbol{D}$. Therefore, we can further eliminate $\boldsymbol{v}$ and equivalently express the constraint (23) as

$$-\gamma \cdot \boldsymbol{D}\mathbf{1} \preceq \boldsymbol{x} \preceq \gamma \cdot \boldsymbol{D}\mathbf{1}. \tag{24}$$

The model (21) can thus be equivalently reformulated as

$$\begin{aligned}
\min_{\boldsymbol{x},\boldsymbol{y},\boldsymbol{B},\boldsymbol{D},\rho} \quad & \rho && \text{(25a)}\\
\text{s.t.} \quad & z(\bar{\boldsymbol{p}}, \bar{\theta}_0) = 1 && \text{(25b)}\\
& |z(\bar{\boldsymbol{p}}, \theta)| \le \rho, \ \forall \theta \in \mathbb{S} && \text{(25c)}\\
& \mathbf{0} \preceq \boldsymbol{D} \preceq \eta \cdot \boldsymbol{B} && \text{(25d)}\\
& \boldsymbol{B}\mathbf{1} \preceq \mathbf{1} && \text{(25e)}\\
& \mathbf{1}^T \boldsymbol{B}\mathbf{1} = N && \text{(25f)}\\
& -\gamma \cdot \boldsymbol{D}\mathbf{1} \preceq \boldsymbol{x} \preceq \gamma \cdot \boldsymbol{D}\mathbf{1} && \text{(25g)}\\
& \boldsymbol{y} = (\mathbf{1} \otimes \boldsymbol{x}) \odot \mathrm{vec}(\boldsymbol{B}) && \text{(25h)}\\
& \boldsymbol{B} \in \{0,1\}^{M \times L}. && \text{(25i)}
\end{aligned}$$

Next, we consider another product constraint (21i) in model (21), which corresponds to constraint (25h) in the above reformulated model. For this purpose, let us denote

$$\boldsymbol{x} = \left[x_1, \cdots, x_M\right]^T \tag{26}$$

$$\boldsymbol{y} = \mathrm{vec}(\boldsymbol{Y}). \tag{27}$$

In (27), $\boldsymbol{Y}$ is an $M \times L$ matrix. When $\boldsymbol{Y}$ and $\boldsymbol{B}$ are blocked by rows, they can be represented as follows:

$$\boldsymbol{Y} = \begin{bmatrix} \boldsymbol{y}_1^T \\ \vdots \\ \boldsymbol{y}_M^T \end{bmatrix}, \boldsymbol{B} = \begin{bmatrix} \boldsymbol{b}_1^T \\ \vdots \\ \boldsymbol{b}_M^T \end{bmatrix}. \tag{28}$$

With the above notations and after performing some manipulations, the constraint (25h) can be equivalently expanded into the following form:

$$\boldsymbol{y}_m = x_m \cdot \boldsymbol{b}_m, \ m = 1, \cdots, M. \tag{29}$$

In (29), x_m is a real variable, and its value lies within the interval $[-\eta\gamma, \eta\gamma]$. The vector $\boldsymbol{b}_m$ is a binary vector, whose elements can only take values of zero or one. Essentially, we need to linearize and reformulate the constraint involving the multiplication of a continuous variable and an integer variable.

Before addressing the nonlinear constraint (29), we first introduce the following lemma, which enables the equivalent linearization of products involving continuous and integer variables. The proof of the lemma can be found in [35].

Theorem 1. *Let z_1 be a real-valued continuous variable belonging to the interval $[l, u]$, and let $z_2 \in \{0,1\}$ be a binary variable. Then the product constraint $z = z_1 z_2$ can be equivalently reformulated as*

$$\begin{aligned}
& z_1 - \bar{K} \cdot (1 - z_2) \le z \le z_1 + \bar{K} \cdot (1 - z_2) && \text{(30a)}\\
& l \cdot z_2 \le z \le u \cdot z_2 && \text{(30b)}\\
& l \le z_1 \le u && \text{(30c)}\\
& z_2 \in \{0,1\} && \text{(30d)}
\end{aligned}$$

where $\bar{K}$ is a sufficiently large positive number, as long as it satisfies $\bar{K} \ge u - l$.

For constraint (29), it can be regarded as an extension of the scalar product form in *Lemma 1*. Based on *Lemma 1*, for a given $m \in \{1, \cdots, M\}$, it is not difficult to reformulate constraint (29) as

$$\begin{aligned}
& x_m \cdot \mathbf{1} - K \cdot (\mathbf{1} - \boldsymbol{b}_m) \le \boldsymbol{y}_m \le x_m \cdot \mathbf{1} + K \cdot (\mathbf{1} - \boldsymbol{b}_m) && \text{(31a)}\\
& -\eta\gamma \cdot \boldsymbol{b}_m \le \boldsymbol{y}_m \le \eta\gamma \cdot \boldsymbol{b}_m && \text{(31b)}\\
& -\eta\gamma \le x_m \le \eta\gamma && \text{(31c)}\\
& \boldsymbol{b}_m \in \{0,1\}^M && \text{(31d)}
\end{aligned}$$

where K is a sufficiently large positive number satisfying $K \ge 2\eta\gamma$. Using the notations from (27) and (28), the aforementioned M sets of constraints can be compactly represented in terms of $\boldsymbol{x}$, $\boldsymbol{y}$ and $\boldsymbol{B}$ as follows:

$$\begin{aligned}
& \boldsymbol{y} \preceq \mathbf{1} \otimes \boldsymbol{x} + K \cdot (\mathbf{1} - \mathrm{vec}(\boldsymbol{B})) && \text{(32a)}\\
& \boldsymbol{y} \succeq \mathbf{1} \otimes \boldsymbol{x} - K \cdot (\mathbf{1} - \mathrm{vec}(\boldsymbol{B})) && \text{(32b)}\\
& \boldsymbol{y} \preceq \eta\gamma \cdot \mathrm{vec}(\boldsymbol{B}) && \text{(32c)}\\
& \boldsymbol{y} \succeq -\eta\gamma \cdot \mathrm{vec}(\boldsymbol{B}) && \text{(32d)}\\
& \boldsymbol{x} \preceq \eta\gamma \cdot \mathbf{1} && \text{(32e)}\\
& \boldsymbol{x} \succeq -\eta\gamma \cdot \mathbf{1} && \text{(32f)}\\
& \boldsymbol{B} \in \{0,1\}^{M \times L}. && \text{(32g)}
\end{aligned}$$

The above constraint (32) represents the linearized reformulation of constraint (25h). This reformulation is exact under the constraint $x_m \in [-\eta\gamma, \eta\gamma]$. We can see that the original product constraint in (25h) has been equivalently replaced.

In fact, considering that $\eta \gg 1$, it is evident that the constraints (32e) and (32f) become redundant in the presence of constraint (25g). Consequently, we can ultimately reformulate the model (21) into the following form:

$$\min_{\boldsymbol{x},\boldsymbol{y},\boldsymbol{B},\boldsymbol{D},\rho} \quad \rho \tag{33a}$$

$$\text{s.t.} \quad z(\bar{\boldsymbol{p}}, \bar{\theta}_0) = 1 \tag{33b}$$
$$|z(\bar{\boldsymbol{p}}, \theta)| \le \rho, \ \forall \theta \in \mathbb{S} \tag{33c}$$
$$\mathbf{0} \preceq \boldsymbol{D} \preceq \eta \cdot \boldsymbol{B} \tag{33d}$$
$$\boldsymbol{B}\mathbf{1} \preceq \mathbf{1} \tag{33e}$$
$$\mathbf{1}^T \boldsymbol{B}\mathbf{1} = N \tag{33f}$$
$$-\gamma \cdot \boldsymbol{D}\mathbf{1} \preceq \boldsymbol{x} \preceq \gamma \cdot \boldsymbol{D}\mathbf{1} \tag{33g}$$
$$\boldsymbol{y} \preceq \mathbf{1} \otimes \boldsymbol{x} + K \cdot (\mathbf{1} - \mathrm{vec}(\boldsymbol{B})) \tag{33h}$$
$$\boldsymbol{y} \succeq \mathbf{1} \otimes \boldsymbol{x} - K \cdot (\mathbf{1} - \mathrm{vec}(\boldsymbol{B})) \tag{33i}$$
$$\boldsymbol{y} \preceq \eta\gamma \cdot \mathrm{vec}(\boldsymbol{B}) \tag{33j}$$
$$\boldsymbol{y} \succeq -\eta\gamma \cdot \mathrm{vec}(\boldsymbol{B}) \tag{33k}$$
$$\boldsymbol{B} \in \{0,1\}^{M \times L} \tag{33l}$$

where $z(\bar{\boldsymbol{p}}, \theta)$ is related to the variables $\boldsymbol{D}$ and $\boldsymbol{y}$, and its expression is given in (20). Compared to model (21), we have excluded variables $\boldsymbol{\delta}$ and $\boldsymbol{v}$ in the above model (33). More importantly, the product constraints have been linearized and reformulated. It can be observed that all the constraints, except for the integer constraint (33l), are convex. The above MIP model (33) is tractable and can be solved using MIP solvers. It is crucial to note that the above linearization is an exact reformulation, not an approximation, and therefore preserves the optimality of the solution to the original model (21).

Let ρ_* denote the objective function value obtained from model (33). It is important to note that while the objective of the array geometry optimization in model (33) is to achieve the lowest possible PSL, the final realized PSL (denoted as $\bar{\rho}$) may be higher than ρ_*. This discrepancy stems from the difference between the actual radiation pattern $|f(\bar{\boldsymbol{p}}, \theta)|$ and the approximated pattern $|z(\bar{\boldsymbol{p}}, \theta)|$ used in the optimization. Our analysis from Section 3.1 shows that

$$|f(\bar{\boldsymbol{p}}, \theta)| \le |z(\bar{\boldsymbol{p}}, \theta)| + r(\theta) \tag{34}$$

where $r(\theta)$ is defined in (9). The above result indicates that the realized PSL $\bar{\rho}$ satisfies

$$\bar{\rho} \le \rho_* + \max_{\theta \in \mathbb{S}} \ r(\theta) \tag{35}$$

Nevertheless, the actual simulation results demonstrate that, the deviation of the final realized PSL $\bar{\rho}$ from the objective function value ρ_* obtained from model (33) is acceptable. On the other hand, the PSL performance can be further enhanced by imposing a more stringent version of constraint (33c):

$$|z(\bar{\boldsymbol{p}}, \theta)| \le \rho - \chi(\theta), \ \forall \theta \in \mathbb{S} \tag{36}$$

where $\chi(\theta)$ denotes the given sidelobe pre-deepening function, the values of which can be specified according to $r(\theta)$.

As a summary, Algorithm 1 outlines the key steps of the proposed array geometry optimization method with phase quantization constraint. It is worth noting that the array geometry optimization model (33) corresponds to the case of single focused-beam synthesis. For scenarios such as phase-only reconfigurable beampattern synthesis and shaped-beam synthesis, model (33) can also be adapted with minor modifications.

Algorithm 1 Array geometry optimization method with phase quantization constraint.

[h]

1: Set up an M-element candidate array with antenna position vector $\bar{\boldsymbol{p}} = [\bar{p}_1, \cdots, \bar{p}_M]^T$.
2: Give $\bar{\theta}_0$, N, η, γ, K, $\boldsymbol{c}$, and $\mathbb{S}$.
3: Solve the problem (33) using an MIP solver, and denote the resulting solution as $\boldsymbol{x}_*$, $\boldsymbol{y}_*$, $\boldsymbol{B}_*$, $\boldsymbol{D}_*$, and ρ_*, respectively.
4: Find all indices i such that $\upsilon_i \neq 0$, and construct a set $\mathbb{G}$ with these indices, where υ_i represents the ith element of vector $\boldsymbol{D}_*\mathbf{1}$.
5: For $\forall i \in \mathbb{G}$, obtain the antenna position $\check{p}_i = \bar{p}_i + x_{*,i}/\upsilon_i$. The corresponding excitation $\iota\check{\upsilon}_i$ is given by the ith entry of the vector $\boldsymbol{D}_*\boldsymbol{c}$.

4. Extensions

In the preceding section, we considered how to optimize the array geometry under phase quantization constraint. Notably, the proposed method can be extended to address a wider range of scenarios. Next, we present several extensions.

4.1. Array geometry optimization with amplitude quantization constraint

As the first extension, we initially delve into the optimization of array geometry considering amplitude quantization constraint. For simplicity, we focus on the scenario of array geometry optimization for amplitude-only low sidelobe synthesis. In this case, we consider J-bit amplitude quantization and jointly design the array geometry and excitation amplitude to achieve the desired low sidelobe beampattern.

By enumerating all candidate excitation amplitudes corresponding to J-bit quantization, we can obtain the following vector $\boldsymbol{h}$:

$$\boldsymbol{h} = [\alpha_1^{(J)}, \cdots, \alpha_{2^J}^{(J)}]^T. \tag{37}$$

To select the excitation amplitudes from $\boldsymbol{h}$, we introduce an $M \times 2^J$ binary matrix $\boldsymbol{B}$. The weight vector under amplitude quantization constraint can be expressed as

$$\boldsymbol{w} = \boldsymbol{B}\boldsymbol{h}. \tag{38}$$

Following (15) and (19), we can similarly derive that

$$\begin{aligned} z(\bar{\boldsymbol{p}}, \theta) &= \boldsymbol{h}^T \boldsymbol{B}^T \boldsymbol{a}(\bar{\boldsymbol{p}}, \theta) + \boldsymbol{h}^T \boldsymbol{B}^T [\boldsymbol{\delta} \odot \boldsymbol{a}'(\bar{\boldsymbol{p}}, \theta)] \\ &= \boldsymbol{h}^T \boldsymbol{B}^T \boldsymbol{a}(\bar{\boldsymbol{p}}, \theta) + \boldsymbol{g}^T \boldsymbol{t}(\bar{\boldsymbol{p}}, \theta) \end{aligned} \tag{39}$$

where

$$\boldsymbol{g} \triangleq (\mathbf{1} \otimes \boldsymbol{\delta}) \odot \mathrm{vec}(\boldsymbol{B}) \tag{40}$$
$$\boldsymbol{t}(\bar{\boldsymbol{p}}, \theta) \triangleq \boldsymbol{h} \otimes \boldsymbol{a}'(\bar{\boldsymbol{p}}, \theta). \tag{41}$$

Our task is to achieve the lowest PSL by optimizing the antenna selection states and their corresponding offsets, which are described by $\boldsymbol{B}$ and $\boldsymbol{\delta}$, respectively. It should be noted that the array response $z(\bar{\boldsymbol{p}}, \theta)$ is directly related to the product of these two optimization variables.

From (39), we can see that the array response is similar to (20) from the previous section. This allows us to apply the same linearization technique to reformulate the product constraint (40). Ultimately, it is not difficult to derive the following MIP model:

$$\min_{\boldsymbol{\delta}, \boldsymbol{g}, \boldsymbol{B}, \rho} \quad \rho \tag{42a}$$
$$\text{s.t.} \quad z(\bar{\boldsymbol{p}}, \bar{\theta}_0) = 1 \tag{42b}$$
$$|z(\bar{\boldsymbol{p}}, \theta)| \le \rho, \ \forall \theta \in \mathbb{S} \tag{42c}$$
$$\boldsymbol{B}\mathbf{1} \preceq \mathbf{1} \tag{42d}$$
$$\mathbf{1}^T \boldsymbol{B}\mathbf{1} = N \tag{42e}$$
$$\boldsymbol{g} \preceq \mathbf{1} \otimes \boldsymbol{\delta} + K \cdot (\mathbf{1} - \mathrm{vec}(\boldsymbol{B})) \tag{42f}$$
$$\boldsymbol{g} \succeq \mathbf{1} \otimes \boldsymbol{\delta} - K \cdot (\mathbf{1} - \mathrm{vec}(\boldsymbol{B})) \tag{42g}$$
$$\boldsymbol{g} \preceq \gamma \cdot \mathrm{vec}(\boldsymbol{B}) \tag{42h}$$
$$\boldsymbol{g} \succeq -\gamma \cdot \mathrm{vec}(\boldsymbol{B}) \tag{42i}$$
$$\|\boldsymbol{\delta}\|_\infty \le \gamma \tag{42j}$$
$$\boldsymbol{B} \in \{0,1\}^{M \times 2^J} \tag{42k}$$

where $z(\bar{\boldsymbol{p}}, \theta)$ is related to the variables $\boldsymbol{B}$ and $\boldsymbol{g}$, and its expression is given in (39). The above formulation is tractable and can be solved using MIP solvers.

Remark 1. The array geometry optimization scenario considering both phase quantization and amplitude quantization can be similarly extended. Let Q and J denote the quantization bits for the excitation phase and amplitude, respectively. Taking into account the potential combinations of different candidate excitation phases and amplitudes,

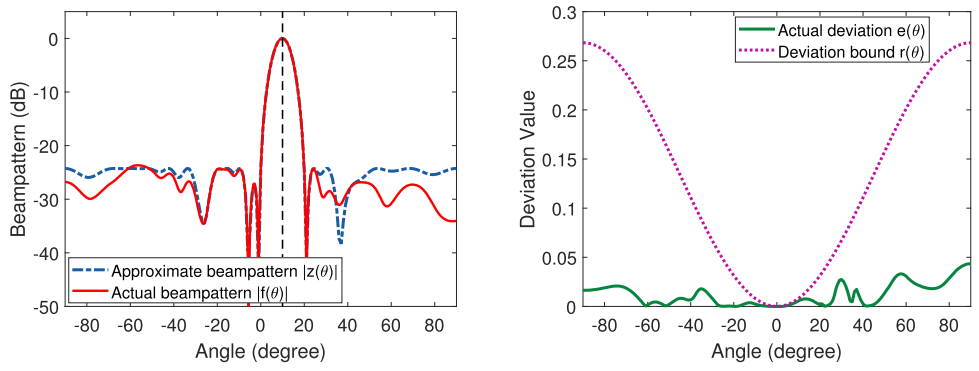

Fig. 3. Simulation results obtained by the proposed method in the scenario of single focused-beam pattern synthesis. (a) Comparison of the approximate beampattern $|z(\theta)|$ with the actual beampattern $|f(\theta)|$. (b) Comparison of the actual beampattern deviation $e(\theta)$ with the deviation bound $r(\theta)$.

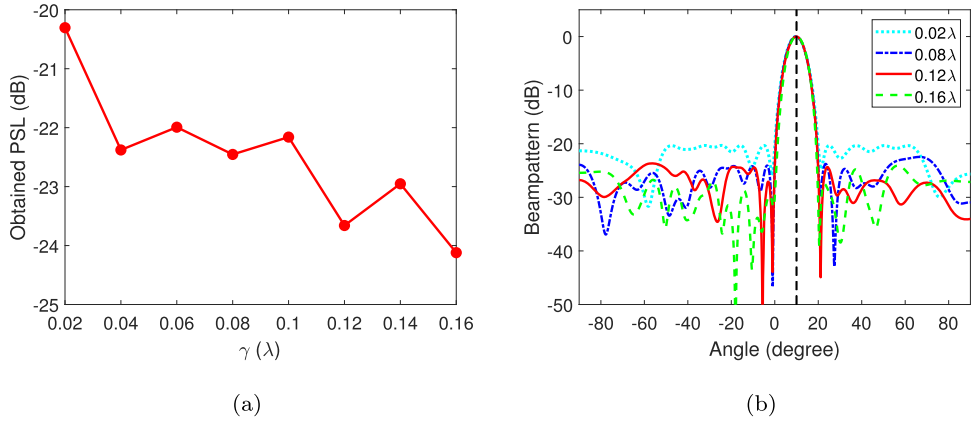

Fig. 4. Simulation results obtained by the proposed method under different values of γ. (a) The curve of obtained PSL versus γ. (b) Comparison of beampatterns obtained under different values of γ.

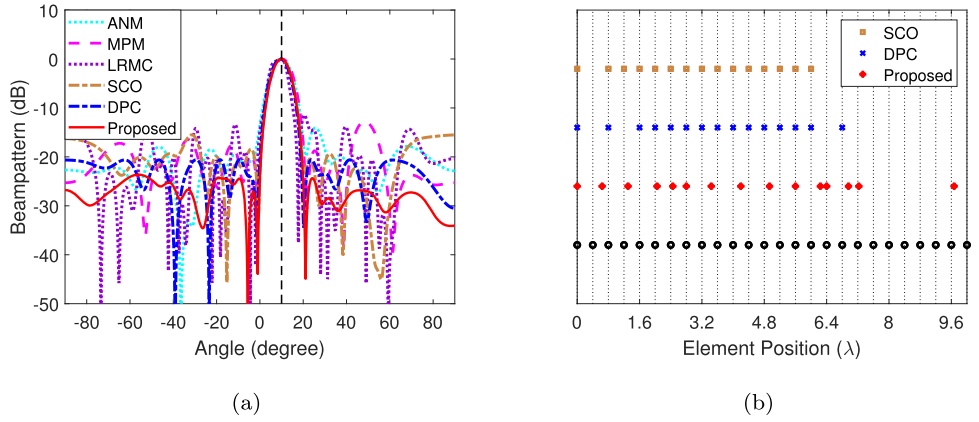

Fig. 5. Simulation comparison in the scenario of single focused-beam pattern synthesis. (a) Comparison of beampattern results. (b) Comparison of array geometry results.

we can introduce the 2^{Q+J}-dimensional vector $\boldsymbol{r} \triangleq \boldsymbol{c} \otimes \boldsymbol{h}$ to encapsulate all feasible excitation candidate states. With the binary matrix $\boldsymbol{B}$, we can express the weight vector as $\boldsymbol{w} = \boldsymbol{B}\boldsymbol{r}$. It is not hard to see that the expression of array response in this case is similar to (39). Therefore, the optimization model considering both phase quantization and amplitude quantization is analogous to the tractable model in (42), with only minor changes in several notations.

4.2. Sparse array optimization and multi-objective design

Besides optimizing the array geometry for a given number of elements, the proposed scheme can be easily extended to sparse array optimization scenarios, thereby achieving the desired beampattern with as few elements as possible. Taking the amplitude-only low sidelobe synthesis scenario discussed in Section 4.1 as an example, suppose we

Table 1
Comparative analysis of different methods.

Method	Aperture	Quantization	Constant Modulus	2-D Array	Flexibility
ANM [23]	Continuous	Not Supported	Not Supported	Not Supported	Low
MPM [8]	Continuous	Not Supported	Not Supported	Not Supported	Low
LRMC [10]	Continuous	Not Supported	Not Supported	Not Supported	Medium
SCO [12]	Discrete	Not Supported	Not Supported	Supported	Medium
DPC [30]	Discrete	Supported	Supported	Supported	Medium
DL [24]	Continuous	Not Supported	Supported	Supported	Low
Proposed	Continuous	Supported	Supported	Supported	High

Table 2
Array geometry and excitation results obtained by the proposed method in single-beam pattern synthesis scenario.

n	$p_n(\lambda)$	$\lvert w_n\rvert$	$\angle w_n$	n	$p_n(\lambda)$	$\lvert w_n\rvert$	$\angle w_n$
1	0	0.0264	45°	9	4.9342	0.1260	315°
2	0.6400	0.0537	45°	10	5.6000	0.0858	0°
3	1.3043	0.0810	90°	11	6.2400	0.0600	0°
4	2.0484	0.1092	135°	12	6.4000	0.0534	90°
5	2.4528	0.0234	225°	13	6.9610	0.0243	45°
6	2.8000	0.1345	180°	14	7.2255	0.0259	135°
7	3.4400	0.1402	225°	15	9.6715	0.0061	315°
8	4.1981	0.1499	270°				

Table 3
Running time comparison of different methods.

Method	ANM	MPM	LRMC	SCO	DPC	Proposed
Time (s)	5	0.6	1045	865	6500	9856

Table 4
Obtained array geometry and the common excitation amplitude in the scenario of phase-only reconfigurable beampattern synthesis.

n	$p_n(\lambda)$	$\lvert w_n\rvert$	n	$p_n(\lambda)$	$\lvert w_n\rvert$	n	$p_n(\lambda)$	$\lvert w_n\rvert$
1	0.048	0.159	9	1.594	0.124	17	7.440	0.103
2	0.280	0.352	10	1.720	0.003	18	8.120	0.045
3	0.447	0.535	11	2.880	0.086	19	8.383	0.060
4	0.595	0.369	12	3.130	0.068	20	8.880	0.009
5	0.880	0.194	13	3.520	0.181	21	9.010	0.094
6	0.920	0.201	14	4.320	0.036	22	9.172	0.051
7	1.280	0.037	15	5.046	0.118	23	9.520	0.031
8	1.320	0.055	16	6.231	0.096	24	9.880	0.019

have pre-assigned a uniform upper bound for sidelobe level (denoted as $\bar{\rho}$). Following (42), we can accomplish geometry optimization for sparse array by simply removing the constraint (42e) and revising the objective function (42a) as

$$\min \quad \mathbf{1}^T \boldsymbol{B}\mathbf{1} \tag{43}$$

Subsequently, the constraint (42c) should be modified as

$$|z(\bar{\boldsymbol{p}}, \theta)| \le \bar{\rho}, \ \forall \theta \in \mathbb{S} \tag{44}$$

which is tractable and can be solved using MIP solvers.

For the above sparse array optimization model, although we can obtain the minimum number of array elements given a specified upper limit on the sidelobe level, the resulting sidelobe level may not be the lowest attainable. In fact, it is possible to refine the model such that both the number of array elements is minimized and the achievable sidelobe level is the lowest, rendering the number of elements and the sidelobe level jointly optimal. This constitutes a multi-objective optimization problem, where we prioritize the minimization of element number and subsequently consider the minimization of PSL.

To accomplish the aforementioned multi-objective optimization design, we reintroduce the variable ρ and impose the following constraints:

$$|z(\bar{\boldsymbol{p}}, \theta)| \le \rho, \ \forall \theta \in \mathbb{S} \tag{45}$$

$$\rho \le \bar{\rho} \tag{46}$$

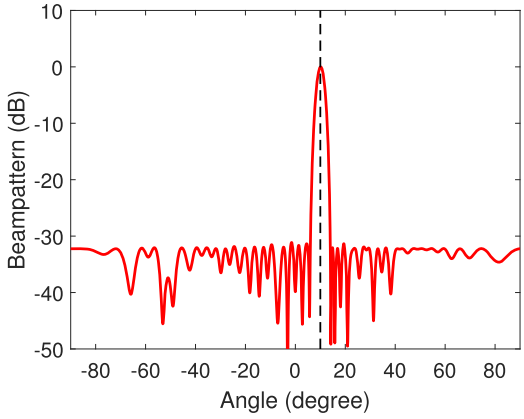

Fig. 6. Beampattern result for large-scale array with $N = 120$.

where ρ is used as a variable to represent the obtained PSL. Within the framework of formulation (33) or (42), the variable ρ must be positive and generally smaller than the normalized mainlobe gain, which is set to one as indicated by (33b) or (42b). In other words, we have $0 < \rho < 1$.

Additionally, it is important to note that $\boldsymbol{B}$ is a binary matrix and the element number (i.e., $\mathbf{1}^T\boldsymbol{B}\mathbf{1}$) changes in discrete steps with a minimal step size of one. Consequently, we can revise the objective function (43) as the following combined version:

$$\min \quad \mathbf{1}^T \boldsymbol{B}\mathbf{1} + \rho \tag{47}$$

In this way, we can attain the minimum PSL while also reducing the element number. This outcome arises because any decrease in the combined objective function resulting from adjustments to $\boldsymbol{B}$ consistently outweighs the variations induced by ρ. Thus, it enables us to prioritize the minimization of element number and subsequently adjust ρ to its minimum.

4.3. Array geometry optimization under constant modulus constraint

In practical array systems, to simplify the design of the RF chain and reduce hardware complexity, the constant modulus constraint can be imposed on the excitations. Under this constraint, the excitation amplitude for each antenna is identical and fixed, thus eliminating the need for variable gain amplifiers or attenuators.

In this case, we need to optimize the array geometry such that all the excitation amplitudes are the same, and the excitation phases meet the given quantization requirements. Considering a Q-bit phase quantization and following the model in (33), we must ensure that all the nonzero elements of $\boldsymbol{D}$ are positive and identical. To obtain this constant-modulus excitation vector, we introduce a scaler variable τ in (33) and add the following constraint:

$$\tau\cdot\mathbf{1}-\eta\cdot(\mathbf{1}-\mathrm{vec}(\boldsymbol{B}))\le\mathrm{vec}(\boldsymbol{D})\le\tau\cdot\mathbf{1}+\eta\cdot(\mathbf{1}-\mathrm{vec}(\boldsymbol{B})). \tag{48}$$

It is evident that if an element of $\boldsymbol{B}$ is one, then the above constraint forces the corresponding element of $\boldsymbol{D}$ to be equal to τ. This ensures that the excitation amplitude of the selected antennas is uniformly equal to τ, thus satisfying the constant modulus constraint. Similar to (33), we can consequently derive a tractable MIP model and solve it using MIP solvers.

4.4. Geometry optimization for planar arrays

The proposed method can be easily extended to the geometry optimization of two-dimensional planar arrays. Given an initial candidate planar array, let the position vectors of the array elements along the x-axis and y-axis be denoted as $\bar{\boldsymbol{p}}_x$ and $\bar{\boldsymbol{p}}_y$, respectively. We can then introduce two separate offset vectors for $\bar{\boldsymbol{p}}_x$ and $\bar{\boldsymbol{p}}_y$, denoting by $\boldsymbol{\delta}_x$ and $\boldsymbol{\delta}_y$,

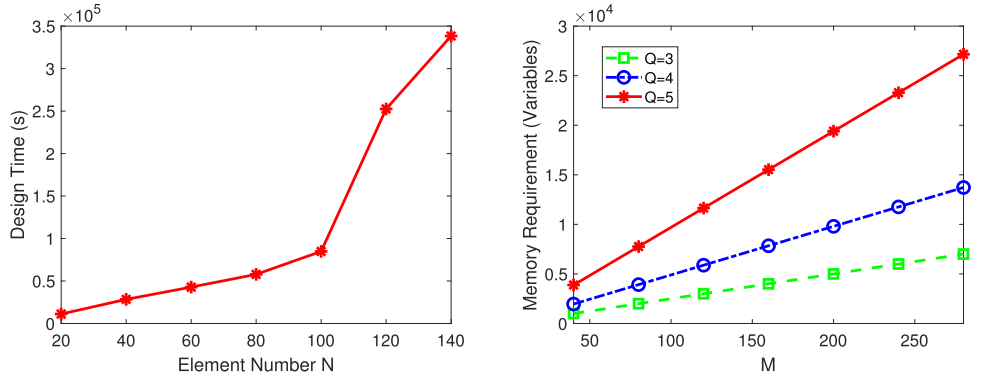

Fig. 7. Results on the complexity of the proposed method. (a) Curve of design time versus the number of elements N. (b) Curve of the number of variables versus the number of candidate elements M.

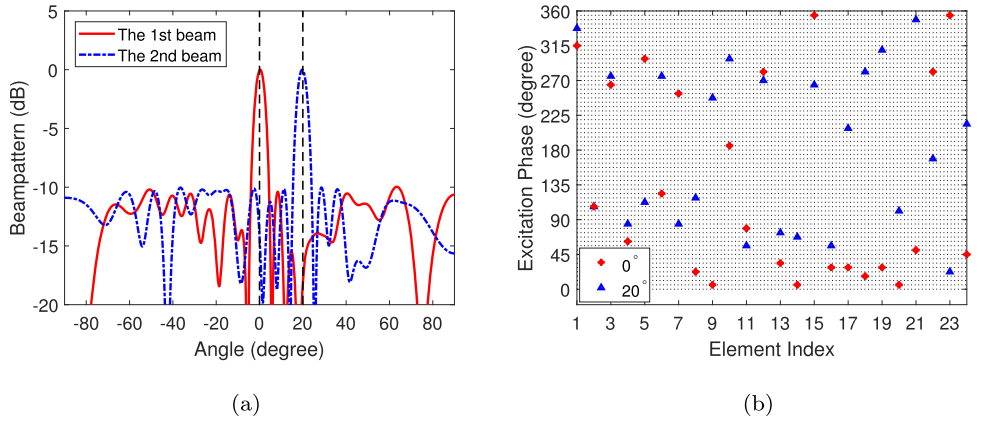

Fig. 8. Simulation results obtained by the proposed method in the scenario of phase-only reconfigurable beampattern synthesis. (a) Obtained beampattern results. (b) Obtained excitation phases for each beam.

respectively. By utilizing the Taylor expansion for a bivariate function, an approximation can be obtained as follows:

$$\boldsymbol{a}(\bar{\boldsymbol{p}}_x+\boldsymbol{\delta}_x,\bar{\boldsymbol{p}}_y+\boldsymbol{\delta}_y,u,v)\approx \boldsymbol{a}(\bar{\boldsymbol{p}}_x,\bar{\boldsymbol{p}}_y,u,v)+\boldsymbol{\delta}_x\odot\boldsymbol{a}'_x(\bar{\boldsymbol{p}}_x,\bar{\boldsymbol{p}}_y,u,v) + \boldsymbol{\delta}_y\odot\boldsymbol{a}'_y(\bar{\boldsymbol{p}}_x,\bar{\boldsymbol{p}}_y,u,v) \tag{49}$$

where $u=cos(\theta)\,cos(\phi)$, $v=cos(\theta)\sin(\phi)$, θ and ϕ represent the elevation angle and azimuth angle, respectively. In the above approximation, $\boldsymbol{a}'_x(\cdot)$ and $\boldsymbol{a}'_y(\cdot)$ are the partial derivative vectors with respect to $\bar{\boldsymbol{p}}_x$ and $\bar{\boldsymbol{p}}_y$, respectively.

Recalling the scenario of geometry optimization for linear arrays, it is evident that the approximation in (49) is a two-dimensional extension to the approximation in (6). Thus, we can imitate the reformulation techniques used for linear arrays to achieve geometry optimization for planar arrays. Also, the geometry optimization for planar arrays is applicable across different scenarios.

5. Comparative analysis and advantages of the proposed method

The main idea and some extensions presented in the preceding sections demonstrate the efficacy of the proposed algorithm. To further elucidate the advantages of the proposed algorithm and provide a clear demarcation from existing methods, we now summarize the key differences as follows.

1. Unlike existing methods that select elements from discrete grids (e.g., the sequential convex optimization (SCO) method in [12], and the sparse array design method with discrete phase constraint (DPC) presented in [30]), the proposed approach enables continuous element selection by introducing continuous position offsets. This thereby introduces greater design degrees of freedom and enables more flexible array design.
2. Unlike existing continuous-position array design methods (e.g., the atomic norm minimization (ANM) method in [23], the matrix pencil method (MPM) in [8], the low-rank matrix completion (LRMC) method in [10]), the proposed method incorporates given excitation quantization constraints directly into the design process. This integrated approach prevents the performance degradation typically associated with post-design quantization.
3. Unlike deep learning-based array design methods (e.g., [24–26]), which require retraining the model for different scenarios or constraints, the proposed method is applicable to various scenarios. It can obtain array design results directly with only simple modifications to the model or constraints, making it more flexible than its deep learning counterparts.

To provide a comprehensive comparison and highlight the advantages of the proposed algorithm, we present a detailed evaluation against existing methods in Table 1.

6. Numerical results

In this section, simulations are presented to demonstrate the effectiveness and superiority of the proposed method. Unless otherwise specified, we use an ULA as the candidate array, and denote μ as the element spacing. When considering quantization for excitation amplitude, we set its dynamic range to 50dB. In all the simulations, we set $\eta=10$

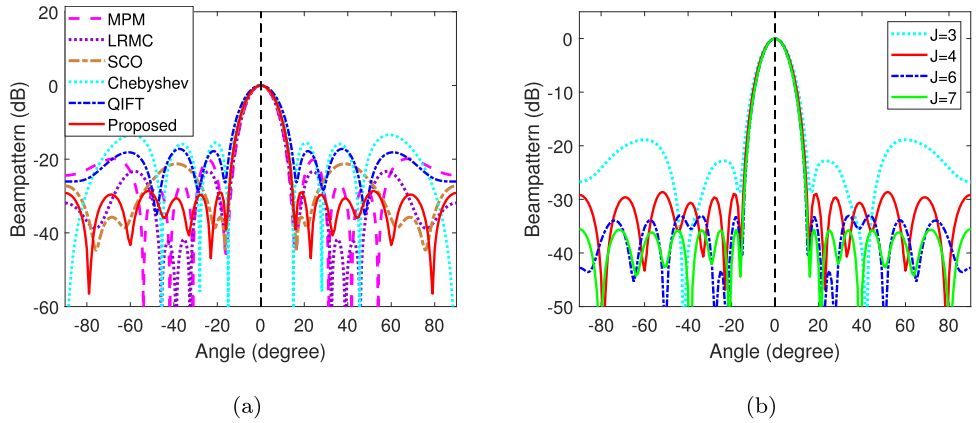

Fig. 9. Simulation comparison in the scenario of amplitude-only low sidelobe synthesis. (a) Comparison of beampatterns with existing algorithms. (b) Beampattern results obtained by the proposed method under different amplitude quantization bits.

Table 5
Obtained array geometry and excitation amplitude in the scenario of amplitude-only low sidelobe synthesis.

n	$p_n(\lambda)$	$\lvert w_n\rvert$(dB)	n	$p_n(\lambda)$	$\lvert w_n\rvert$(dB)
1	0	-23.3333	5	2.6688	-23.3333
2	0.7900	-16.6667	6	3.2336	-13.3333
3	1.5882	-13.3333	7	4.0048	-16.6667
4	2.3359	-13.3333	8	4.8025	-23.3333

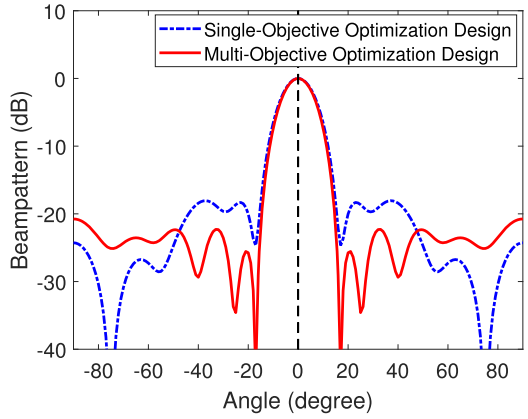

Fig. 10. Comparison of beampatterns obtained by single-objective and multi-objective sparse array designs.

Table 6
Array geometry optimization result with phase and amplitude quantization.

n	$p_n(\lambda)$	n	$p_n(\lambda)$	n	$p_n(\lambda)$	n	$p_n(\lambda)$
1	0	4	1.3997	7	2.7606	10	4.5294
2	0.4240	5	1.7703	8	3.1752		
3	0.9611	6	2.2500	9	3.5695		

Table 7
Array geometry and excitation phase results obtained by the proposed method in the scenario of constant-modulus beampattern synthesis.

n	$p_n(\lambda)$	$\angle w_n$	n	$p_n(\lambda)$	$\angle w_n$
1	0	123.75°	7	2.9685	78.75°
2	0.3098	315.00°	8	3.5149	22.50°
3	0.5685	101.25°	9	3.9643	292.50°
4	1.0257	315.00°	10	4.6991	236.25°
5	1.7923	247.50°	11	5.1431	123.75°
6	2.3661	157.50°	12	5.8572	56.25°

and $K = 20\gamma$. The proposed MIP models are solved by Gurobi [31]. The simulations are conducted using a computing platform, the processor is intel(R) Core(TM) i7-10750H CPU @ 2.60GHz.

6.1. Array geometry optimization with phase quantization constraint

In the first example, we consider array geometry optimization under phase quantization constraint for various beampattern synthesis scenarios.

6.1.1. Array geometry optimization for single focused-beam pattern synthesis

In the first case, we consider array geometry optimization with single focused beam. The candidate array contains $M = 30$ element with spacing $\mu = 0.4\lambda$. We set $Q = 3$, $\gamma = 0.12\lambda$. The mainlobe axis is steered to $\bar{\theta}_0 = 10°$ and the first null width is set to 20°. With the number of array elements set to $N = 15$, our objective is to achieve a PSL as low as possible through the optimization of array geometry, as described by the formulation (33).

To illustrate the effectiveness of the proposed method, particularly the impact of the approximation made in (6), Fig. 3(a) contrasts the resultant beampattern $|f(\bar{\boldsymbol{p}}, \theta)|$ with the approximate beampattern $|z(\bar{\boldsymbol{p}}, \theta)|$ from the optimization model. For the actual beampattern, the PSL is -26.78dB, while for the approximate beampattern, the PSL is -24.26dB, indicating similar PSL values for both. Although there are some discrepancies between $|z(\bar{\boldsymbol{p}}, \theta)|$ and $|f(\bar{\boldsymbol{p}}, \theta)|$ in regions far from the array normal, the levels of the actual beampattern are generally lower than those of the approximate beampattern. Fig. 3(b) compares the actual beampattern deviation (see $e(\theta)$ in (8)) with the upper bound of the deviation (see $r(\theta)$ in (9)). As predicted, $e(\theta)$ is less than $r(\theta)$. In fact, we observe that $e(\theta)$ is significantly lower than $r(\theta)$ at most angles. The array position arrangement and the resulting excitation phase/amplitude obtained by the proposed method are provided in Table 2.

To further evaluate the impact of γ on the proposed method, Fig. 4(a) illustrates the variation curve of the obtained PSL versus γ. It can be observed that as γ increases, the PSL generally exhibits a decreasing trend. It is important to note that the curve is not strictly monotonically decreasing. This is because a larger γ leads to higher design freedom but also introduces greater approximation errors. The resulting PSL is influenced comprehensively by both the design freedom and the approximation errors. Fig. 4(b) presents the beampattern results obtained by the proposed method under several different values of γ.

For comparison purpose, we compare the proposed method with the atomic norm minimization (ANM) method in [23], the matrix pencil method (MPM) in [8], the low-rank matrix completion (LRMC) method in [10], the sequential convex optimization method in [12], and the

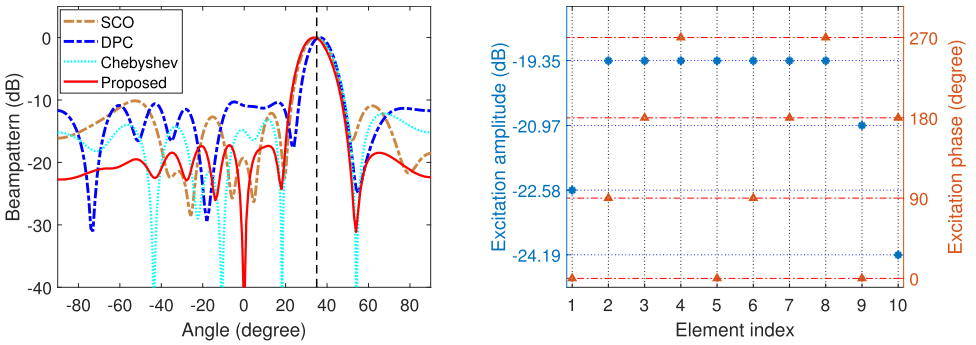

(a) (b)

Fig. 11. Simulation results with phase and amplitude quantization. (a) Comparison of beampattern results. (b) Obtained excitation phases and amplitudes by the proposed method.

sparse array design method with discrete phase constraint (DPC) presented in [30]. Fig. 5 shows the results of the proposed method with those of the comparison methods. Under the same phase quantization bits ($Q = 3$), Fig. 5(a) displays the radiation beampattern results of different methods. It can be observed that existing methods exhibit poor sidelobe levels when phase quantization is considered, and may even suffer from distortions on mainlobe. Fig. 5(b) presents the corresponding array geometry optimization results. As shown, the element arrangements of both the SCO method and the DPC method are on the grid of candidate position. For the proposed method, it introduces position offsets and allows the element positions to be distributed between the grid points. Table 3 compares the running times of different methods. It can be observed that the running time of the proposed method is longer than those of the other methods.

To verify the applicability of our algorithm to large-scale arrays, we configured the parameters with $M = 180$, $N = 120$, and set the first null width to 4°, while keeping all other references unchanged. The resulting beam pattern, presented in Fig. 6, achieves a PSL of -31.2 dB. Furthermore, to evaluate the computational complexity, Fig. 7(a) and (b) depict the scaling of the design time with the number of elements N, and the number of variables with the number of candidate elements M, respectively. The curves confirm that both the time and space complexity of the proposed algorithm increase gradually with the array scale.

6.1.2. Array geometry optimization for phase-only reconfigurable beampattern synthesis

In the second case, we consider array geometry optimization in the scenario of phase-only reconfigurable beampattern synthesis. In this case, we set $M = 50$, $\delta = 0.2\lambda$, $Q = 6$, $\gamma = 0.08\lambda$. The element number of the ultimate array is $N = 24$. For simplicity, we consider two scanning beams steering to 0°, and 20°, respectively. Our task is to jointly design the element positions, excitation phases, and amplitudes such that the overall PSL of the two beams is minimized. Since we are performing phase-only scanning, the excitation amplitudes for all beams should be identical, and the excitation phases should satisfy the given quantization requirement.

Fig. 8(a) presents the beampattern results obtained by the proposed method after 10,000 seconds of execution. Fig. 8(b) illustrates the excitation phases for each beam. It can be observed that the resulting beampatterns by the proposed method are satisfactory, and the excitation phases meet the phase quantization constraint. The obtained array position results and the common excitation amplitude results are presented in Table 4. The PSL obtained by the proposed method is -9.7dB, which is lower than the -8.3dB achieved by the DPC method. This is primarily because the DPC method performs antenna selection on the given grid, whereas the proposed method not only selects antennas but also designs their positions offsets.

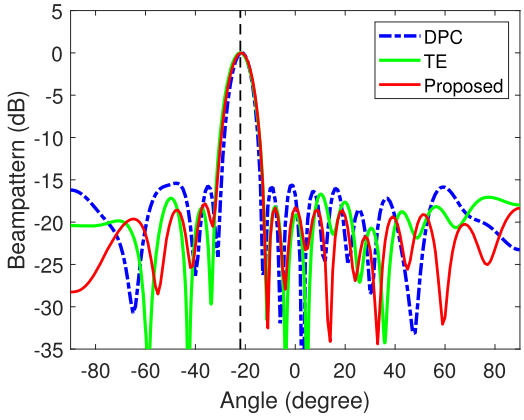

Fig. 12. Comparison of beampattern results in the scenario of constant-modulus beampattern synthesis.

6.2. Array geometry optimization with amplitude quantization constraint

In the second example, we consider array geometry optimization under amplitude quantization constraint for various beampattern synthesis scenarios.

6.2.1. Array geometry optimization for amplitude-only low sidelobe synthesis

In the first case, we consider array geometry optimization for amplitude-only low sidelobe synthesis. The task is to achieve the desired low sidelobe beampattern by designing only the excitation amplitude under quantization constraint. We set $M = 20$, $\delta = 0.4\lambda$, $J = 4$, $\gamma = 0.15\lambda$. The mainlobe axis is steered to $\bar{\theta}_0 = 0°$ and the first null width is set to 30°. With the number of array elements set to $N = 8$, our objective is to achieve a PSL as low as possible through the optimization of array geometry, as described in the formulation (42).

Fig. 9(a) presents a comparison of the beampatterns between the proposed method and existing methods, given the same number of array elements and quantization bits. It can be observed that the proposed method exhibits significantly lower PSL compared to the existing ones. The obtained array position results and the excitation amplitude results are presented in Table 5. To further evaluate the impact of quantization bits on the performance of the proposed method, Fig. 9(b) compares the beampattern results obtained under different amplitude quantization bits. It is evident that a higher quantization bit leads to a lower PSL.

6.2.2. Sparse array optimization and multi-objective design

In the second scenario, we apply the proposed method for sparse array optimization and multi-objective design, as discussed in Section 4.2.

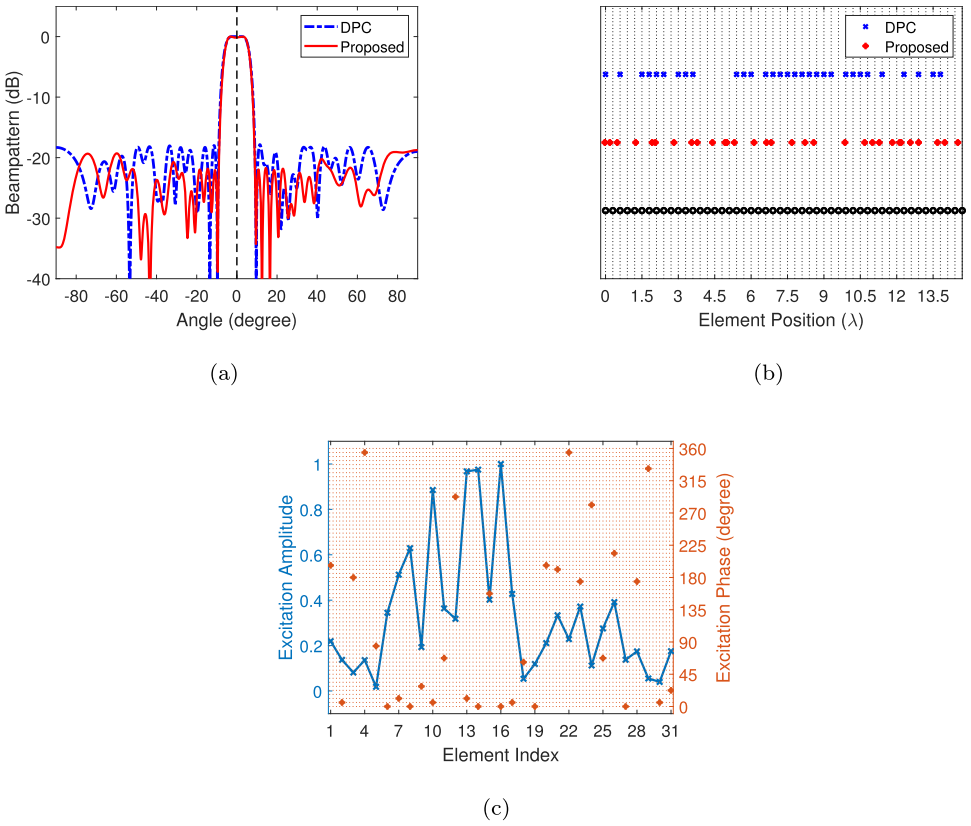

Fig. 13. Simulation results for shaped-beam pattern synthesis. (a) Comparison of beampattern results. (b) Comparison of array geometry results. (c) Obtained excitation phases and amplitudes by the proposed method.

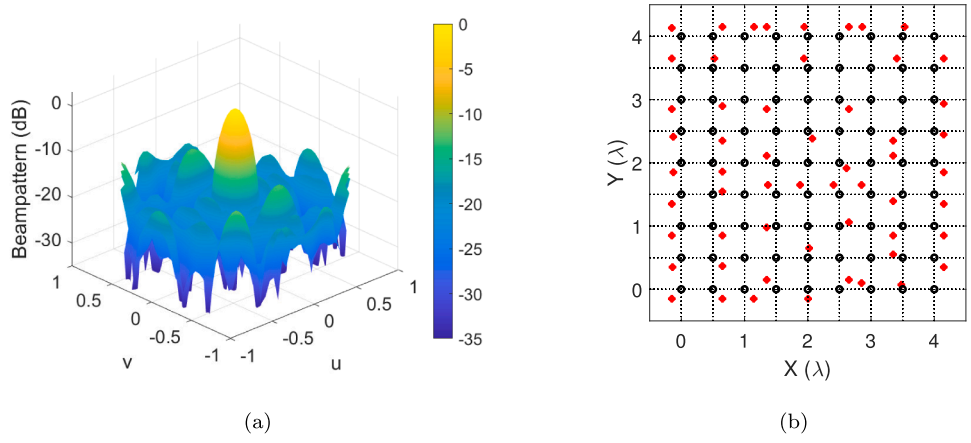

Fig. 14. Simulation results obtained by the proposed method for planar array geometry optimization. (a) Obtained beampattern result. (b) Obtained array geometry result (the black dots and red dots correspond to the candidate array and the array geometry result obtained by the proposed method, respectively).

In this simulation, we specify a upper bound for sidelobe level as −17dB, with other parameters remaining unchanged with the previous simulation. Under the constraints of amplitude-only excitation and amplitude quantization, our objective is to satisfy the above requirements using the minimum number of array elements, as given by the single-objective cost function (43). At the same time, we consider a multi-objective optimization model with the objective function (47), which aims to optimize both the element number and the ultimate PSL. Fig. 10 illustrates the beampatterns resulting from the above two approaches. It can be observed that the beampatterns from both approaches meet the given PSL requirement. Although the two approaches yield sparse arrays with the same element number ($N = 6$), the PSL achieved through multi-objective optimization (−20.75dB) is lower than that obtained from the single-objective optimization (−18.06dB).

6.3. Array geometry optimization in other scenarios

In the third example, we present several other array geometry optimization scenarios to illustrate the wide applicability of the proposed method.

6.3.1. Array geometry optimization with phase and amplitude quantization

The proposed method can be easily applied to array geometry optimization scenarios that consider both phase quantization and amplitude

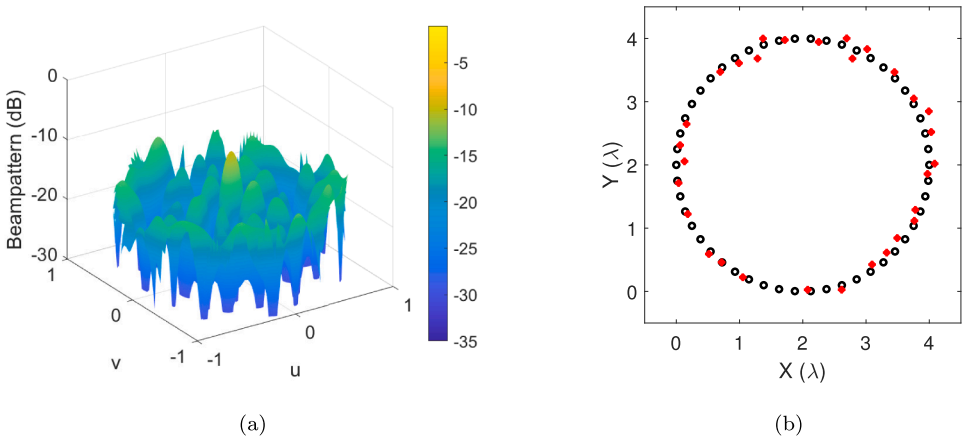

Fig. 15. Simulation results obtained by the proposed method for circular array. (a) Obtained beampattern result. (b) Obtained array geometry result (the black dots and red dots correspond to the candidate array and the array geometry result obtained by the proposed method, respectively).

quantization. We set $M = 20$, $N = 10$, $\delta = 0.4\lambda$, $\gamma = 0.15\lambda$. The mainlobe axis is steered to $\bar{\theta}_0 = 35°$ and the first null width is set to 30°. With a phase quantization bit number of $Q = 2$ and an amplitude quantization bit number of $J = 5$, Fig. 11(a) compares the resulting beampatterns obtained by minimizing the PSL using different methods. The proposed method achieves a PSL of -17.21dB, which is lower than the results obtained by the DPC method (-10.32dB), the SCO method (-10.13dB), and the Chebyshev beampattern (-13.14dB). Fig. 11(b) shows the results of excitation phase and amplitude obtained by the proposed method, and Table 6 presents the array position distribution. The effectiveness of the proposed method for array geometry optimization with phase and amplitude quantization can thus be validated.

6.3.2. Array geometry optimization under constant modulus constraint

Following the discussions in Section 4.3, we now assess the performance of the proposed method on array geometry optimization under constant modulus constraint. We set $M = 30$, $N = 12$, $\delta = 0.4\lambda$, $Q = 5$, $\gamma = 0.12\lambda$. The mainlobe axis is steered to $\bar{\theta}_0 = -22°$ and the first null width is set to 20°. Our task is to achieve a PSL as low as possible by jointly optimizing the array geometry, excitation phases (under quantization constraint), and excitation amplitudes (under constant modulus constraint). With the same simulation conditions, Fig. 12 compares the beampattern results of the proposed method with those of the DPC method in [30] and the Taylor expansion (TE) method in [18]. The PSL of the proposed method is -17.84dB, which is lower than both the DCP method (-15.17dB) and the TE method (-16.52dB). Table 7 lists the array position distribution and excitation phases obtained by the proposed method.

6.3.3. Array geometry optimization for shaped-beam pattern synthesis

To further demonstrate the applicability of the proposed method in shaped-beam synthesis scenario, we take a flat-top beam as the desired beampattern and minimize the PSL through array geometry optimization. In this scenario, we set the center angle of the flat-top beam as 0°. The ripple and width of the mainlobe beam are 0.2dB and 10°, respectively. To optimize the array geometry, we set $M = 50$, $N = 31$, $\delta = 0.3\lambda$, $Q = 6$, with other configurations remaining the same as in the previous simulation. Fig. 13(a) illustrates the beampattern result of the proposed method and compares it with the DPC method from [30]. Under the same phase quantization bits, the PSL of the proposed method is -19.26dB, which is lower than that of the DPC method (-17.84dB). Fig. 13(b) compares the array geometry results obtained from the two methods, and Fig. 13(c) presents the excitation phases and amplitudes obtained by the proposed method.

6.3.4. Geometry optimization for planar arrays

To verify that the proposed method can optimize the array geometry for planar arrays, we consider a two-dimensional array scenario and set $M = 81$, $N = 56$, $\delta = 0.5\lambda$, $\gamma = 0.15\lambda$. The mainlobe axis is steered to the normal direction. With an amplitude quantization bit number of $J = 5$ and after 20,000 seconds of execution, Fig. 14 shows the two-dimensional beampattern result and array geometry result obtained by the proposed method. In this case, the resulting PSL is -17.4 dB.

To further validate the performance of the proposed algorithm for other types of two-dimensional array distributions, we employed a uniform circular array with $M = 50$ elements as the candidate array. With the number of elements set to $N = 30$ and all other parameters unchanged, the proposed algorithm yields the radiation pattern and array layout depicted in Fig. 15. In this case, the resulting PSL is -13.5 dB. The wide applicability of the proposed method can thus be verified.

7. Conclusions

In this paper, we have presented a framework for array geometry optimization under excitation quantization constraints using mixed-integer programming. Our work specifically addresses the challenge of designing arrays with phase and/or amplitude quantization limits applied to the excitation. By jointly designing antenna selection states and position offsets, we have developed a continuous antenna selection scheme for array geometry optimization. Our method is versatile and applicable to both one-dimensional linear arrays and two-dimensional planar arrays, accommodating various constraint scenarios and supporting multi-objective array geometry design. We have investigated linearization and equivalent reformulation techniques to transform the array geometry optimization problems into tractable MIP models. These models can be efficiently solved using standard MIP solvers, making our approach practical for real-world applications. Theoretical analysis has been provided to validate the rationality of our methodology. We have conducted extensive simulations to demonstrate the effectiveness and superiority of the proposed method across various scenarios. The results show that our approach consistently outperforms existing methods, achieving better array geometry designs for the given quantization configuration.

CRediT authorship contribution statement

Xue Shi: Writing, Software, Validation, Project administration, Writing – original draft; **Xuejing Zhang:** Conceptualization, Methodology; **Cheng Liu:** Investigation, Visualization; **Xuepan Zhang:** Project administration, Funding acquisition.

Data availability

Data will be made available on request.

Declaration of competing interest

The authors declare that they have no known competing financial interests or personal relationships that could have appeared to influence the work reported in this paper.

Appendix A. Proof of (9)

According to the expressions of $z(\bar{\boldsymbol{p}},\theta)$ and $f(\bar{\boldsymbol{p}},\theta)$, we can obtain

$$e(\theta) = \left||z(\bar{\boldsymbol{p}},\theta)| - |f(\bar{\boldsymbol{p}},\theta)|\right| \tag{A.1a}$$

$$\le \left|z(\bar{\boldsymbol{p}},\theta) - f(\bar{\boldsymbol{p}},\theta)\right| \tag{A.1b}$$

$$= \left|\boldsymbol{w}^T[\boldsymbol{a}(\bar{\boldsymbol{p}}+\boldsymbol{\delta},\theta) - \boldsymbol{a}(\bar{\boldsymbol{p}},\theta) - \boldsymbol{\delta}\odot\boldsymbol{a}'(\bar{\boldsymbol{p}},\theta)]\right| \tag{A.1c}$$

$$= \left|\boldsymbol{w}^T\left(\frac{\boldsymbol{a}''(\boldsymbol{\xi},\theta)}{2}\odot\boldsymbol{\delta}\odot\boldsymbol{\delta}\right)\right| \tag{A.1d}$$

$$= \frac{2\pi^2\sin^2(\theta)}{\lambda^2}\left|\boldsymbol{w}^T[\boldsymbol{a}(\boldsymbol{\xi},\theta)\odot\boldsymbol{\delta}\odot\boldsymbol{\delta}]\right| \tag{A.1e}$$

$$\le \frac{2\pi^2\sin^2(\theta)}{\lambda^2}\|\boldsymbol{w}\|_{\beta_1}\cdot\|[\boldsymbol{a}(\boldsymbol{\xi},\theta)\odot\boldsymbol{\delta}\odot\boldsymbol{\delta}]\|_{\beta_2} \tag{A.1f}$$

$$= \frac{2\pi^2\sin^2(\theta)}{\lambda^2}\|\boldsymbol{w}\|_{\beta_1}\cdot\|\boldsymbol{\delta}\odot\boldsymbol{\delta}\|_{\beta_2} \tag{A.1g}$$

where $\boldsymbol{\xi} = [\xi_1,\cdots,\xi_M]$ is a vector satisfying $\bar{\boldsymbol{p}} \preceq \boldsymbol{\xi} \preceq \bar{\boldsymbol{p}}+\boldsymbol{\delta}$, β_1 and β_2 can be any positive numbers as long as they satisfy $\frac{1}{\beta_1}+\frac{1}{\beta_2}=1$. In the above derivation, (A.1b) utilizes the triangle inequality, (A.1d) employs the Taylor's mean value theorem, (A.1f) leverages the Hölder inequality, and (A.1g) makes use of the fact that $|\boldsymbol{a}(\boldsymbol{\xi},\theta)| = \mathbf{1}$. Moreover, the inequality (A.1b) holds with equality if and only if

$$\angle z(\bar{\boldsymbol{p}},\theta) = \angle f(\bar{\boldsymbol{p}},\theta). \tag{A.2}$$

The inequality (A.1f) holds with equality if and only if the following conditions are satisfied:

$$\sin(\angle\boldsymbol{w} + \angle\boldsymbol{a}(\boldsymbol{\xi},\theta)) = \mathbf{0} \tag{A.3}$$

$$\chi|w_m|^{\beta_1} = \delta_m^{2\beta_2},\ m=1,\cdots,M \tag{A.4}$$

where χ is a real value. This completes the proof of (9).

References

[1] P. Rocca, G. Oliveri, R.J. Mailloux, A. Massa, Unconventional phased array architectures and design methodologies-A review, Proc. IEEE 104 (3) (2016) 544–560.

[2] A. Gupta, U. Madhow, A. Arbabian, A. Sadri, Design of large effective apertures for millimeter wave systems using a sparse array of subarrays, IEEE Trans. Signal Process. 67 (24) (2019) 6483–6497.

[3] S. Sun, Y.D. Zhang, 4D Automotive radar sensing for autonomous vehicles: a sparsity-oriented approach, IEEE J. Sel. Top. Signal Process. 15 (4) (2021) 879–891.

[4] M. Huan, J. Liang, Y. Ma, W. Liu, Y. Wu, Y. Zeng, Optimization of high-resolution and ambiguity-free sparse planar array geometry for automotive MIMO radar, IEEE Trans. Signal Process. 72 (2024) 4332–4348.

[5] V. Murino, A. Trucco, C.S. Regazzoni, Synthesis of unequally spaced arrays by simulated annealing, IEEE Trans. Signal Process. 44 (1) (1996) 119–122.

[6] M.M. Khodier, C.G. Christodoulou, Linear array geometry synthesis with minimum sidelobe level and null control using particle swarm optimization, IEEE Trans. Antennas Propag. 53 (8) (2005) 2674–2679.

[7] K. Chen, X. Yun, Z. He, C. Han, Synthesis of sparse planar arrays using modified real genetic algorithm, IEEE Trans. Antennas Propag. 55 (4) (2007) 1067–1073.

[8] Y. Liu, Z. Nie, Q.H. Liu, Reducing the number of elements in a linear antenna array by the matrix pencil method, IEEE Trans. Antennas Propag. 56 (9) (2008) 2955–2962.

[9] G. Oliveri, A. Massa, Bayesian compressive sampling for pattern synthesis with maximally sparse non-uniform linear arrays, IEEE Trans. Antennas Propag. 59 (2) (2011) 467–481.

[10] X. Zhang, T. Gu, Synthesis of sparse linear arrays via low-rank Hankel matrix completion, IEEE Trans. Antennas Propag. 72 (12) (2024) 9522–9527.

[11] S. Boyd, L. Vandenberghe, Convex Optimization, Cambridge, U.K., Cambridge Univ. Press, 2004.

[12] B. Fuchs, Synthesis of sparse arrays with focused or shaped beampattern via sequential convex optimizations, IEEE Trans. Antennas Propag. 60 (7) (2012) 3499–3503.

[13] P. You, Y. Liu, S. Chen, K. Xu, W. Li, Q. Liu, Synthesis of unequally spaced linear antenna arrays with minimum element spacing constraint by alternating convex optimization, IEEE Antennas Wireless Propag. Lett. 16 (2017) 3126–3130.

[14] S.E. Nai, W. Ser, Z.L. Yu, H. Chen, Beampattern synthesis for linear and planar arrays with antenna selection by convex optimization, IEEE Trans. Antennas Propag. 58 (2010) 3923–3930.

[15] D. Pinchera, M.D. Migliore, F. Schettino, M. Lucido, G. Panariello, An effective compressed-sensing inspired deterministic algorithm for sparse array synthesis, IEEE Trans. Antennas Propag. 66 (1) (2018) 149–159.

[16] Y. Aslan, J. Puskely, A. Roederer, A. Yarovoy, Multiple beam synthesis of passively cooled 5G planar arrays using convex optimization, IEEE Trans. Antennas Propag. 68 (5) (2020) 3557–3566.

[17] R.C. Nongpiur, D.J. Shpak, Synthesis of linear and planar arrays with minimum element selection, IEEE Trans. Signal Process. 62 (20) (2014) 5398–5410.

[18] B. Fuchs, A. Skrivervik, J.R. Mosig, Synthesis of uniform amplitude focused beam arrays, IEEE Antennas Wireless Propag. Lett. 11 (2012) 1178–1181.

[19] O.M. Bucci, M. Urso, T. Isernia, P. Angeletti, G. Toso, Deterministic synthesis of uniform amplitude sparse arrays via new density taper techniques, IEEE Trans. Antennas Propag. 58 (6) (2010) 1949–1958.

[20] J.M.E. Geerarts, G. Theis, A.B. Smolders, D. Caratelli, Constrained deterministic synthesis of conformal supershaped antenna arrays, IEEE Trans. Antennas Propag. 71 (11) (2023) 8726–8738.

[21] D. Caratelli, M.C. Vigano, A novel deterministic synthesis technique for constrained sparse array design problems, IEEE Trans. Antennas Propag. 59 (11) (2011) 4085–4093.

[22] S. Yang, B. Liu, Z. Hong, Z. Zhang, Low-complexity sparse array synthesis based on off-grid compressive sensing, IEEE Antennas Wireless Propag. Lett. 21 (12) (2022) 2322–2326.

[23] Z. Wang, G. Sun, J. Tong, Y. Ji, Pattern synthesis for sparse linear arrays via atomic norm minimization, IEEE Antennas Wireless Propag. Lett. 20 (12) (2021) 2215–2219.

[24] N. Sarker, P. Podder, M.R.H. Mondal, S.S. Shafin, J. Kamruzzaman, Applications of machine learning and deep learning in antenna design, optimization, and selection: a review, IEEE Access 11 (2023) 103890–103915.

[25] D. Lin, Y. Lu, L. Maman, J. Earls, A. Boag, P. Baldi, Optimization of antenna array configurations using deep learning, IEEE Open J. Antennas Propag. 6 (5) (2025) 1367–1374.

[26] S.A. Hamza, M.G. Amin, Sparse array design for optimum beamforming using deep learning, IEEE Trans. Aerosp. Electron Syst. 60 (1) (2024) 133–144.

[27] T.H. Ismail, Z.M. Hamici, Array pattern synthesis using digital phase control by quantized particle swarm optimization, IEEE Trans. Antennas Propag. 58 (6) (2010) 2142–2145.

[28] S.K. Goudos, Antenna design using binary differential evolution: application to discrete-valued design problems, IEEE Antennas Propag. Mag. 59 (1) (2017) 74–93.

[29] W.P.M.N. Keizer, Low sidelobe phased array pattern synthesis with compensation for errors due to quantized tapering, IEEE Trans. Antennas Propag. 59 (12) (2011) 4520–4524.

[30] D. Xia, X. Zhang, Synthesis of sparse arrays with discrete phase constraints via mixed-integer programming, IEEE Antennas Wireless Propag. Lett. 23 (3) (2024) 1030–1034.

[31] Gurobi Optimizer Reference Manual, Gurobi Optimization, Briarwood, Texas, USA, 2023.

[32] IBM ILOG CPLEX Optimization Studio CPLEX Users Manual, IBM, Raleigh, NC, USA, 2018.

[33] S. Lee, H.J. Song, Accurate statistical model of radiation patterns in analog beamforming including random error, quantization error, and mutual coupling, IEEE Trans. Antennas Propag. 69 (7) (2021) 3886–3898.

[34] S.P. Chepuri, G. Leus, Continuous sensor placement, IEEE Signal Process. Lett. 22 (5) (2015) 544–548.

[35] G. Chen, C. Wang, X. Zhang, J. Gong, M. Tan, Probabilistically robust joint transmit code and receive filter design for extended targets: a mixed-integer programming approach, IEEE Trans. Aerosp. Electron. Syst. 61 (2) (2025) 2503–2515.